AIAA JOURNAL
Vol. 35, No. 3, March 1997

Discrete Vortex Method for Simulating Unsteady Flow Around Pitching Aerofoils

Hequan Lin,* Marco Vezza,[†] and R. A. McD. Galbraith[‡]
University of Glasgow, Glasgow G12 8QQ, Scotland, United Kingdom

A modified discrete vortex method to simulate the separated flow around an aerofoil undergoing pitching motion is described. The vorticity generated in the thin layer around the body is discretized into vortices in accordance with the multipanel surface representation. By convection and diffusion the vortices are released from the body and advanced in the wake as determined by the Biot–Savart law and random-walk model, respectively. Both unsteady static and pitching cases are presented, and comparison with the test data illustrates that, without prior knowledge of the developing separation and reattachment points for the model, good agreement has been achieved.

Nomenclature

A = area of body (section)
B = volume within the body
c = aerofoil chord
F_b = volume within the control zone
F_w = volume outside the control zone
K = number of subpanels for each panel
$\boldsymbol{k}$ = unit vector
k = reduced pitch rate $k = \Omega c / 2V$
l = panel length
m = index number of subpanel within the panel
N = number of panels for the body
P = static pressure
Re = Reynolds number
$\boldsymbol{r}$, r = position vector and its magnitude
S = surface of the body
$\boldsymbol{s}$, $\boldsymbol{n}$ = unit vector along and normal to the surface
t = time
$\boldsymbol{U}$ = flow velocity
V = velocity
Z = position in the form of complex number
z = vortex position in the form of complex number
α = angle of attack
Γ = circulation
γ = circulation density
Δt = time step
δ = distance of nascent vortex off the body
ν = kinematic viscosity
ρ = fluid density
σ = vortex core radius
$\boldsymbol{\Psi}$, Ψ = vector potential and stream function
Ω = rotational velocity
ω = vorticity

Subscripts

c = reference point for the body motion
i = index for body, index for vortices outside the control zone
j = index for panel
m = index for subpanel, moment
n = nascent vortices, normal component
s = surface velocity
t = tangential component

I. Introduction

THE flowfield around a pitching aerofoil, especially the phenomenon of dynamic stall, has been attracting intensive research in recent decades.[1,2] The perceived benefits of the research apply, for example, to helicopters, high-agility fighter aircraft, and wind turbines. In the case of the helicopter, the main rotor blade section operates in a periodic aerodynamic environment during forward flight.

Experimental studies[3–5] show that the physical phenomena characterizing dynamic stall and static stall are very different. Massive separation from the upper surface, the formation of a primary dynamic vortex and its subsequent convection and diffusion dominate the dynamic stall flow. This indicates that successful numerical analysis is dependent upon accurate simulation of the vortex behavior.

In recent years, various numerical models have been developed to study dynamic stall. Most of the models are based on the solution of the Navier–Stokes equations. Different schemes are in use: the O-grid scheme combined with the Joukowsky transformation,[6] the Moving O-grid scheme,[7] the hybrid grid scheme (dynamic structured and unstructured grid),[8] viscous/inviscid interaction schemes,[9] and the random-walk vortex method coupled with the von Mises transform.[10] Among these, the discrete vortex method,[10–12] also based on the Navier–Stokes equations, has the advantages of being highly adaptive and grid free. The method is particularly suitable for simulating dynamic stall, where the vortex dominates the flow and grid generation becomes more intricate in order to match the moving boundary and capture the vortex structure.

In this paper, a discrete vortex scheme is developed to solve the stream function-vorticity formulation of the Navier–Stokes equations for a pitching aerofoil. Unlike other schemes,[10,11] neither a transform mapping nor prespecification of the separation point is required. A thin layer near the aerofoil, referred to as the control zone, is the source of the vortices. Vorticity arises from the no-slip condition on the solid boundary. A Lagrangian scheme is used to describe the vortices released from the control zone, and the random-walk method[12] is employed to simulate diffusion. The surface of the body is discretized into main panels and subpanels, the latter used to represent the leading edge accurately and to define the vorticity within the control zone. The boundary condition is satisfied by enforcing zero mass flow through the main panels. Three cases are presented in the paper pertaining to the NACA0015: impulse start unsteady static at 10 deg, ramp-up from 0 to 40 deg, and ramp-up ramp-down. Comparisons with the experimental results[13] available at Glasgow University show good agreement.

II. Governing Equations

Two-dimensional incompressible flow is governed by the following continuity and full viscous Navier–Stokes equations:

$$\nabla . \boldsymbol{U} = 0 \tag{1}$$

$$\frac{\mathrm{D}\boldsymbol{U}}{\mathrm{D}t} = -\frac{1}{\rho}\nabla P + \nu\nabla^2 \boldsymbol{U} \tag{2}$$

Received Oct. 27, 1995; revision received Nov. 23, 1996; accepted for publication Dec. 1, 1996; also published in *AIAA Journal on Disc*, Volume 2, Number 2.

*Postgraduate, Department of Aerospace Engineering.

[†] Lecturer, Department of Aerospace Engineering.

[‡] Shoda Professor, Head, Department of Aerospace Engineering. Member AIAA.

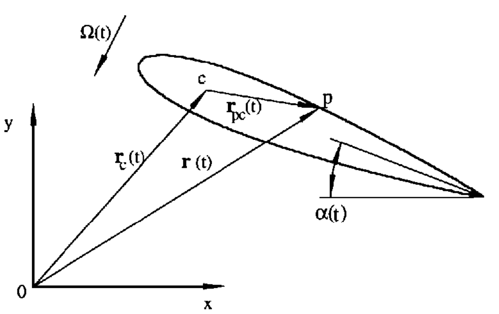

Fig. 1 Reference coordinate system.

By using the definitions of vorticity $\omega = \nabla \times U$ with $\omega = k\omega$, vector potential Ψ with $U = \nabla \times \Psi$, $\Psi = k\Psi$, $\nabla \cdot \Psi = 0$, and rotational velocity $\Omega_i = k\Omega_i$, the governing equations can be expressed in vorticity/stream function form:

$$\nabla^2 \Psi = -\omega \tag{3}$$

$$\frac{D\omega}{Dt} = \nu \nabla^2 \omega \tag{4}$$

where subscript i is the index for the body.

The velocity field within the area of the body, depicted in Fig. 1, corresponds to that of a solid region with reference point c:

$$U_i = U_{ic} + \Omega_i \times (r - r_{ic}) \tag{5}$$

or in the stream function form

$$\nabla^2 \Psi_i = -2\Omega_i \tag{6}$$

The velocity at the point p outside the solid region is governed by Eqs. (1–4). The relationship between the velocity and the vorticity has been derived previously[14]:

$$\begin{aligned} U_p = U_\infty &+ \frac{1}{2\pi}\int_{F_b} \omega \frac{k \times (r_p - r)}{\|r_p - r\|^2}\, \mathrm{d}F_b \\ &+ \frac{1}{2\pi}\int_{F_w} \omega \frac{k \times (r_p - r)}{\|r_p - r\|^2}\, \mathrm{d}F_w \\ &+ \frac{1}{2\pi}\int_{B_i} 2\Omega_i \frac{k \times (r_p - r)}{\|r_p - r\|^2}\, \mathrm{d}B_i \end{aligned} \tag{7}$$

where $F = F_b \cup F_w$ and $F_b \cap F_w = 0$.

The equation details the four contributions to the velocity from the freestream, the vorticity in the small control area around the solid region (control zone), the vorticity in the remaining flow area, and the vorticity inside the solid region due to the motion of the body.

Flow in the far field is undisturbed, whereas the no-slip condition on the body requires the velocity of flow particles to be equal to that of the surface. These conditions can be expressed either in velocity or stream function form:

$$U = U_i \quad \text{on} \quad S_i \quad \text{and} \quad U = U_\infty \quad \text{on} \quad S_\infty \tag{8}$$

$$\nabla \Psi = \nabla \Psi_i \quad \text{on} \quad S_i \quad \text{and} \quad \nabla \Psi = \nabla \Psi_\infty \quad \text{on} \quad S_\infty \tag{9}$$

III. Numerical Implementation

For a two-dimensional body, a polygonal representation of the body surface is created by connecting node points with a straight line to form a series of panels. N main node points are located on the body that define N plane panels approximating the N curved segments of the surface. Each curved segment is further subdivided into K equal-length subpanels by the specification of $K - 1$ nodes along the segments.

The thin area near the body surface is regarded as a special zone, the control zone, in which the vorticity is created. The vorticity in the rest of the flowfield arises through convection and diffusion of that generated in the control zone. The discretization of vorticity in the control zone can be regarded as a two-stage process.

First, the total vorticity within the control zone, γ, is treated as a quantity that varies piecewise linearly and continuously along the surface. The values of γ at main node points therefore represent the whole surface distribution.

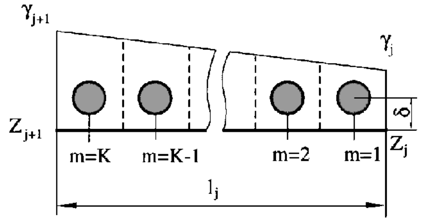

Fig. 2 Discretization and γ distribution.

Second, the panel distribution of total vorticity is further broken down into vortex blobs, one for each subpanel. The blob is positioned a distance δ directly above the middle of the subpanel. The discretization is illustrated in Fig. 2. Each blob is assumed to have a symmetrical vorticity distribution, described by a core function that corresponds to the velocity distribution[11]:

$$v(r) = \frac{\Gamma}{2\pi}\frac{r}{r^2 + \sigma^2}$$

where Γ is the total blob circulation and r is the distance of a point from the blob center.

The boundary condition on the surface is implemented by ensuring zero mass flow through each panel. Although this implementation cannot guarantee the equations to be fulfilled at every point, there is at least one point on each panel with zero relative normal velocity. The implementation is expressed as

$$F_{js} + F_{ji} + F_{jf} + F_{jv} + F_{jn} = 0 \tag{10}$$

with each term representing the contribution of mass flow by different sources. The first and second terms, F_{js} and F_{ji}, are from the motion of the body and are thus additional items to those for the static case, F_{jf}, F_{jv}, and F_{jn}, representing the contributions by the freestream, the vortices outside the control zone, and the vortices within the control zone. The latter are regarded as nascent vortices.

All vortices outside the control zone originate from nascent vortices. Their positions are the result of convection and diffusion at each time step. Their circulations are unchanged with time. At the beginning of the calculation, the total number of such vortices is zero, as is the corresponding contribution to the mass flow.

The total number of equations (10) is N for a body with N panels, but only $N - 1$ are independent because there is no source or sink within the body. Hence after $N - 1$ panels satisfy zero mass flow, the mass flow for the final panel will automatically be zero.

A further equation required to make the solution unique is obtained from Kelvin's theorem. The circulation of the vortices in the entire flowfield remains constant because there is no external source of vorticity. For each body, the additional condition is

$$\sum_v \Gamma_v + \sum_{j=1}^{N}\sum_{m=1}^{K} (\Gamma_j)_m + 2\Omega_i A_i = \Gamma_{\mathrm{st}} \tag{11}$$

where the first term is the circulation of vortices in the wake, the second is the circulation of the nascent vortices, the third is the circulation due to the body rotation, and the fourth is the initial circulation in the flowfield prior to the start of calculations. The second term contains the unknown γ values.

The strength of the nascent vortices are obtained once the equations are solved for the $N\gamma$ values.

The simulation of vorticity convection and diffusion employs an operator splitting technique, where the vorticity transport equation (4) is split into a separate convection part $D\omega/Dt = 0$ and diffusion part $\partial\omega/\partial t = \nu\nabla^2\omega$, both of which are solved sequentially as proposed in reference.[12] The convection equation, as for inviscid flows, describes the invariance of vorticity as it moves with the fluid. The velocity of convection is therefore the same as that of the associated flow particle and is determined from Eq. (7) using the discretized vorticity representation. At each time step, only the velocity at the vortex locations is needed to advance the simulation.

The solution of the diffusion part is based on the diffusion of a unit point vortex in two dimensions, given by

$$\omega(r) = (1/4\pi\nu t)e^{-r^2/4\nu t}$$

This is also the Gaussian probability density of random variables x and y in two dimensions, with zero mean and standard deviation of $\sqrt{(2\nu t)}$, which can be numerically simulated by the random-walk method. The method adds additional random displacements η_x, η_y at each time step in the x and y directions to the convection displacements. The random numbers are generated numerically by computers and satisfy the Gaussian distribution of zero mean and standard deviation $\sqrt{(2\Delta t/Re)}$ in dimensionless form.

The Adams–Bashforth second-order method is employed to solve the convection equation, and hence the vortex positions for the next time step are determined, in complex notation, from

$$z_i(t+\Delta t) = z_i(t) + \left[\tfrac{3}{2}V_i(t) - \tfrac{1}{2}V_i(t-\Delta t)\right]\cdot\Delta t + (\eta_x + i\eta_y) \tag{12}$$

for the vortices outside the control zone, whereas only the first-order scheme is used for the nascent vortices. That is,

$$z_i(t+\Delta t) = z_i(t) + V_i(t)\cdot\Delta t + (\eta_x + i\eta_y) \tag{13}$$

The vortices within the control zone are treated separately from those outside, the latter retaining their individual identity. Those within the control zone at the new time are combined with the vorticity created by the surface during this time step, forming the next layer of nascent vortices. Their strengths are determined by implementing the above equations. The process is one of vortex release and absorption and is depicted in Fig. 3.

The number of vortices outside the control zone increases as the computation proceeds. Because the computational cost of the vortex interactions is of $\mathcal{O}(N_v^2)$, where N_v is the number of vortex particles, a vortex merging mechanism is employed, in which two vortices are combined into one if certain criteria are satisfied. In particular, the difference in velocity at the body surface induced by the vortices before and after merging is minimized while maintaining total circulation. Significant merging occurs in the far wake where the effect on the body is very small. Further cost reductions are planned via the implementation of a fast algorithm. The total number of vortices present depends on the complexity of the flow, with only a few hundred for an aerofoil at low incidence but several thousand after separation. Most of the vortices during a computation are located near the body because of the merging scheme employed.

Operating with $\boldsymbol{n}\times$ on the Navier–Stokes Eq. (2) applied to the body surface, an equation for pressure gradient is obtained:

$$\frac{1}{\rho}\frac{\partial P}{\partial s} = -\boldsymbol{s}\cdot\frac{\mathrm{D}\boldsymbol{U}}{\mathrm{D}t} + \nu\frac{\partial\omega}{\partial n} \tag{14}$$

where the normal vector $\boldsymbol{n}$ and the tangential vector $\boldsymbol{s}$ are related by $\boldsymbol{n} = \boldsymbol{s}\times\boldsymbol{k}$.

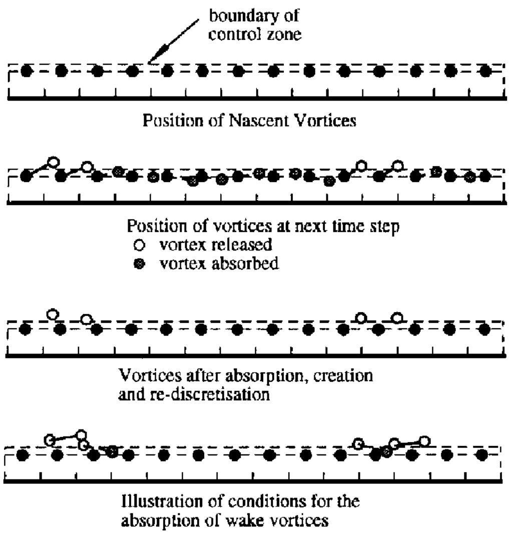

Fig. 3 Illustration of vortex release and absorption.

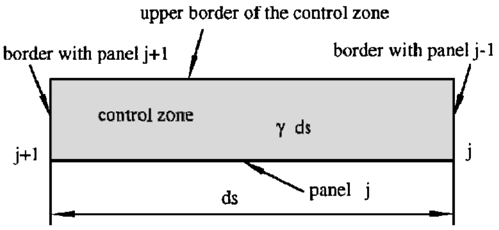

Fig. 4 Vorticity inside the control zone.

Because of the no-slip condition, the flow velocity on the surface should be the same as that of the surface itself, given by Eq. (5). Hence the equation (dropping index i) becomes

$$\frac{1}{\rho}\frac{\partial P}{\partial s} = -\boldsymbol{s}\cdot\frac{\mathrm{D}\boldsymbol{U}_c}{\mathrm{D}t} - \boldsymbol{n}\cdot(\boldsymbol{r}-\boldsymbol{r}_c)\frac{\mathrm{D}\Omega}{\mathrm{D}t} + \boldsymbol{s}\cdot(\boldsymbol{r}-\boldsymbol{r}_c)\Omega^2 + \nu\frac{\partial\omega}{\partial n} \tag{15}$$

The first three terms on the right-hand side of Eq. (15) only appear when the body is in motion and describe the surface tangential components of the acceleration of the reference point, the rotational acceleration, and the centripetal acceleration.

Rewriting the vorticity transport equation (4) as

$$\frac{\mathrm{D}\omega}{\mathrm{D}t} = \frac{\partial\omega}{\partial t} + (\boldsymbol{U}\cdot\nabla)\omega = -\nabla\cdot(-\nu\nabla\omega) \tag{16}$$

$-\nu\nabla\omega$ is the vorticity flux, which, when applied at the body, produces the surface flux $-\boldsymbol{n}\cdot\nu\nabla\omega = -\nu\partial\omega/\partial n$. Therefore, the last term in Eq. (14) can be regarded as the negative vorticity creation rate at the surface.

Consider a control area with one side on part of the body surface and the opposite side on the upper part of the control zone (Fig. 4). The control area has size ds along the surface and moves with the body. The circulation of vortices inside the control area at time t, excluding the vorticity created by the surface at this time, is γ^a ds. This includes the vorticity in existence there at time $t-\Delta t$ and the vorticity flux through the area boundaries (excluding the body surface) from $t-\Delta t$ to t. The circulation of vortices created at the element of surface during this time step is $(-\nu\partial\omega/\partial n)\,\mathrm{d}s\Delta t$. The net circulation of vortices inside this area, γ ds, is given by the sum of these contributions, that is,

$$\left(-\nu\frac{\partial\omega}{\partial n}\right)\mathrm{d}s\Delta t + \gamma^a\,\mathrm{d}s = \gamma\,\mathrm{d}s \tag{17}$$

so

$$\nu\frac{\partial\omega}{\partial n} = \frac{\gamma^a - \gamma}{\Delta t} \tag{18}$$

where γ^a is the equivalent circulation density of existing vortices in the control area at time t and is approximated piecewise linearly in the same fashion as the net vorticity γ.

The integrals from pressure gradient to pressure distribution and from the pressure to aerodynamic force and moment are standard.

IV. Results and Discussion

The model has been used to predict some separated flows. The results for starting flow around a NACA0015 undergoing various motions are presented, including impulse start, ramp-up motion, and ramp-up ramp-down triangle motion.

The aerofoil surface was represented by 80 panels, with 5 subpanels defined between successive main node points. The surface is represented by nearly equal-length panels except close to the leading edge where panel density is increased. Core radius, vortex creation distance above the surface, and size of control zone are empirically specified and are of the same order of magnitude.

Case 1: α = 10-deg Impulse-Start Unsteady Static Flow (Attached Flow)

Figure 5 illustrates the vortex patterns for this case, the two frames corresponding to times shortly after the impulse start and after the flow around the aerofoil has settled. The Reynolds number is $Re = 9.9\times10^6$. From the earlier frame, the vortices are seen to be emitting from the trailing edge and rolling up. This represents the

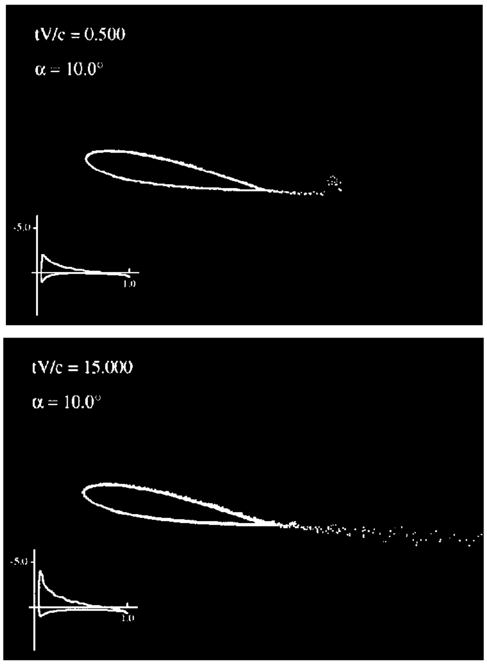

Fig. 5 Vortex pattern of the NACA0015 in impulsive flow at $\alpha = 10$ deg.

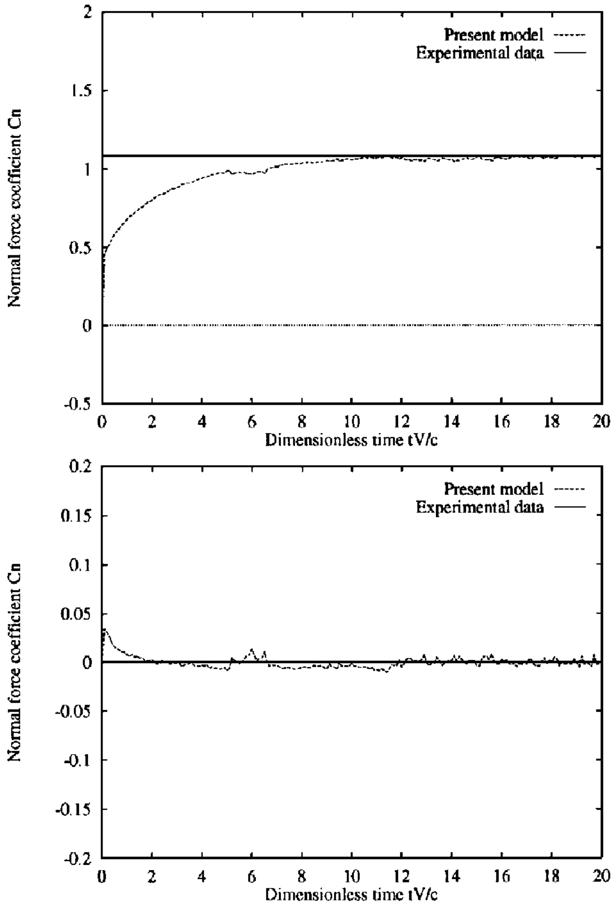

Fig. 6 Characteristics for the NACA0015 at $\alpha = 10$ deg.

starting vortex, and during this period, circulation is built up around the aerofoil. The later frame shows the settled vortex pattern, with vortices again emitting from the trailing edge but no longer rolling up. This is because the vortices trailing from both the upper and the lower surfaces are of opposite sign and almost the same magnitude. At this stage there is little overall change in the circulation around the aerofoil. Also evident is the close proximity of the emerging vortices to the aerofoil surface. This is in good accordance with the established knowledge that the steady flow for this case is attached.

The time histories of the normal force and pitching-moment coefficients C_n vs tV/c (dimensionless time), $C_{m1/4}$ vs tV/c are presented in Fig. 6. These illustrate the classic features of starting flow, i.e., an initial impulse followed by a gradual buildup to steady-state values corresponding to the increasing circulation that develops around the aerofoil. This process is consistent with the frames in Fig. 5, where the starting vortex can be seen to be carrying circulation downstream. The circulation around the body surface increases to maintain constancy of total circulation.

Also in Fig. 6 is the experimental C_n, which has been reduced from published steady-state test data.[15] It is apparent that, after the initial transient has died away, the predicted C_n approaches very close to the test result.

Case 2: Ramp-Up

Four frames are presented in Fig. 7 for the case of a ramp change in angle of attack from -1 to 40 deg, at $Re = 9.9 \times 10^6$ and reduced pitch rate $k = 0.0487$. The starting and the ending phases of the motion are modeled as an acceleration and deceleration, as shown in Fig. 8, in which the time history is the same as that for the experiment. The first frame shows the attached flow at an angle

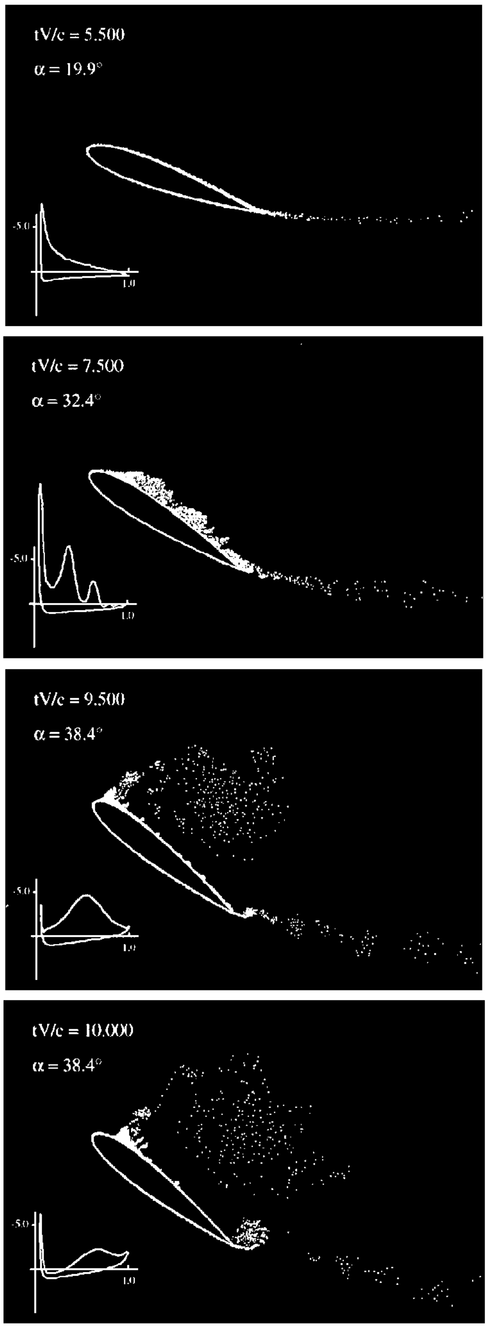

Fig. 7 Vortex pattern of the NACA0015 during ramp-up motion.

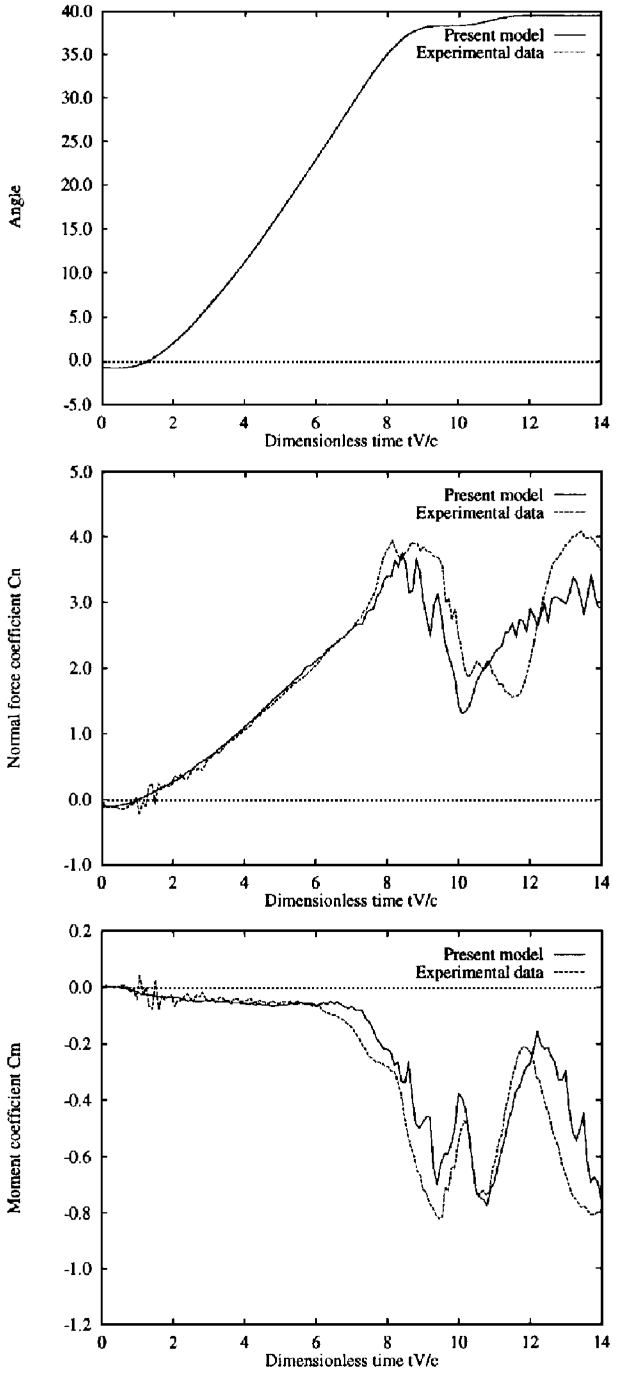

Fig. 8 Characteristics for the NACA0015 during ramp-up motion.

higher than the static stall value. In the second frame, in which dimensionless time $tV/c = 7.5$ and $\alpha = 32.4$ deg, the main dynamic vortex is formed near the leading edge upon the upper surface and, correspondingly, the suction pressure is increased there. In addition, the secondary vortex is simulated. As time advances, the third frame indicates that the dynamic vortex is transported along the surface and finally in the fourth it has detached from the aerofoil and a countervortex is formed over the trailing edge.

Angle of attack α time history, C_n vs tV/c (dimensionless time), and $C_{m1/4}$ vs tV/c are presented in Fig. 8, together with the test results. The overall agreement is fairly good; however, the differences that do occur are discussed in the following paragraph.

A high level of fidelity is achieved during the attached flow phase, which extends to angles of incidence well beyond the static stall value. Beyond this point the model predicts a slightly lower C_n gradient and peak C_n. This means that the suction effect of the dynamic stall vortex measured in the experiment has not been completely simulated. Although this could be due to the core function and radius employed, which affect to some degree the formation and progress of the dynamic stall vortex, it is also possible that wind-tunnel blockage is influential during this event, which deforms the outer flow significantly. In keeping with current practice for dynamic stall experiments, the data were not corrected for wind-tunnel blockage because of the lack of known correction technique for such unsteady test cases. In addition, the empirical parameters, for example, the creation distance δ, are not linked directly to the flow conditions in the current model, although future plans are to incorporate such a link. The earlier separation indicated by the experiment is illustrated very clearly in the $C_{m1/4}$ diagram, although the peak levels are generally in good agreement.

The ramp-up case was run on a Silicon Graphics machine, with one 150-MHz IP22 processor, and took around 500 min of CPU time to perform 2000 time steps, most of which corresponded to postseparation conditions. The number of vortices ranged from a few hundred to around 4000, depending on the flow conditions.

Case 3: Ramp-Up and Ramp-Down

In Fig. 9 there are four frames for ramp-up and ramp-down, with two for each motion stage. They are accompanied by the angle of

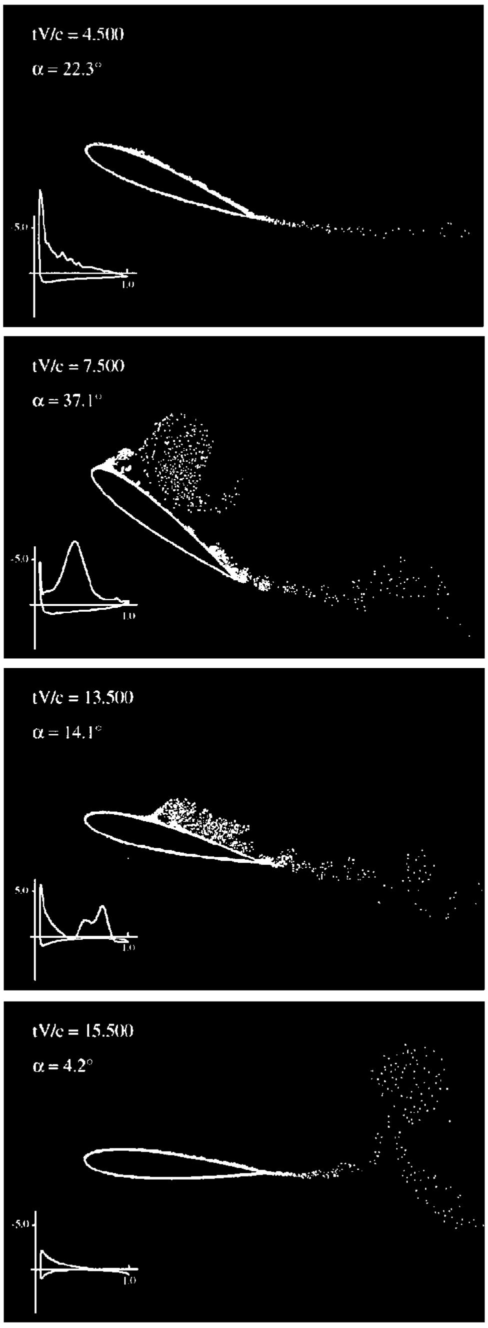

Fig. 9 Vortex pattern of the NACA0015 during ramp-up and ramp-down.

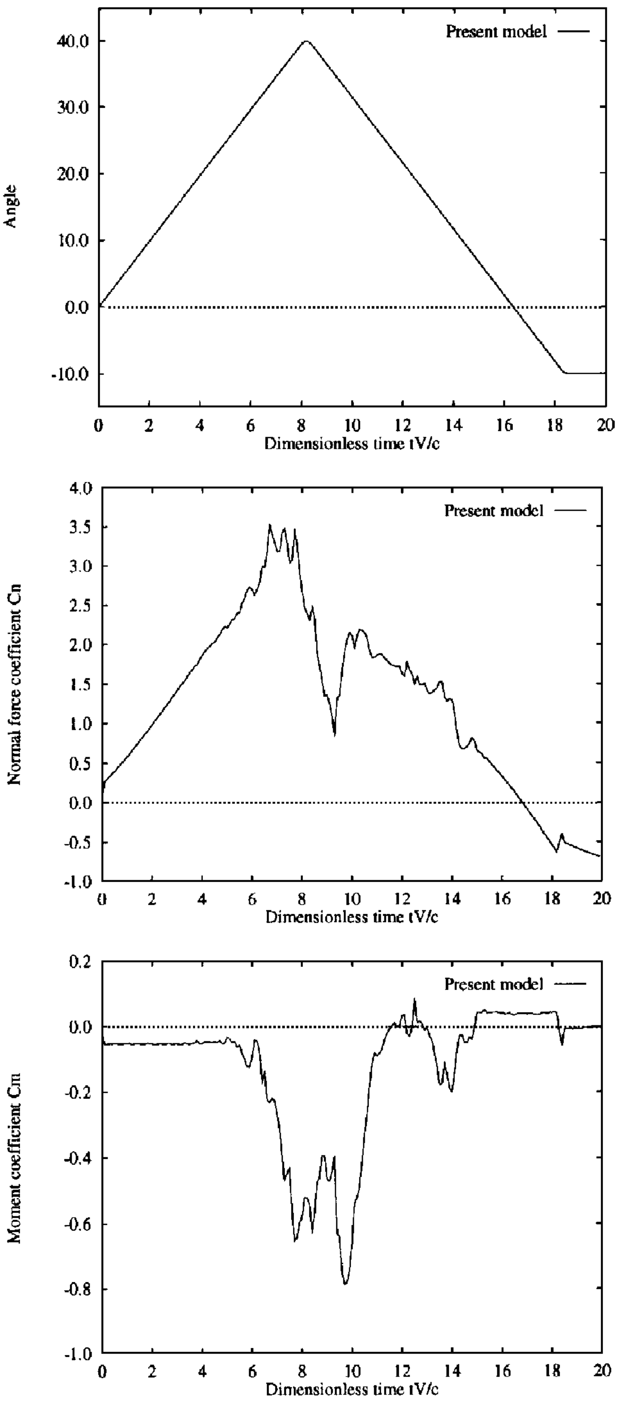

Fig. 10 Characteristics for the NACA0015 during ramp-up and ramp-down.

attack αtime history, C_n vs tV/c, and $C_{m1/4}$ vs tV/c in Fig. 10. The angle of attack is increased from 0 to 40 deg and then is reduced to −10 deg at reduced pitch rate $k = 0.0487$ for each case. Reynolds number $Re = 9.9\times10^6$. Frame 1 shows that the flow is still attached at high angles of attack, and frame 2 presents the separation from the leading edge during the pitching-up process. Frame 3 shows that the separation point is moving rearward, and the final frame illustrates the flow fully attached.

The characteristic hystereses in the aerodynamic loads are predicted. Of particular importance is the reduction in C_n during ramp down. During ramp-up the processes are virtually identical to those described in the preceding case. However, the delay in reattachment and lack of vortex lift during ramp-down results in lower C_n values. Although upper-surface suction starts to build up during ramp-down at higher incidence, this process is undermined by the continual reduction in incidence and possibly by the influence of the vortex system previously shed.

V. Conclusion

A discrete vortex model has been developed that predicts separated, incompressible flows without specification of separation points. The agreement with the test data shows that the introduction of the control zone and multipanel discretization of the vorticity around the body has enabled the modeling of separated flows like those around pitching aerofoils. It is anticipated that future developments, in particular the incorporation of exterior constraints, more correlations between the flow conditions and the numerical parameters, and turbulence effects, will further improve the prediction capabilities of the model.

Acknowledgments

The first author acknowledges the Committee of Vice-Chancellors and Principals for its financial support through the Overseas Research Students Awards Scheme. The authors would like to thank F. Coton and R. Green of the Department of Aerospace Engineering for their friendly and very useful discussion and E. Leitch for her assistance in obtaining the test data.

References

[1] McCroskey, W. J., "Unsteady Airfoils," *Annual Review of Fluid Mechanics*, Vol. 14, 1982, pp. 285–311.

[2] Carr, L. W., "Progress in Analysis and Production of Dynamic Stall," *Journal of Aircraft*, Vol. 25, No. 1, 1988, pp. 6–17.

[3] Walker, J. M., Helin, H. E., and Strickland, J. H., "An Experimental Investigation of an Airfoil Undergoing Large-Amplitude Pitching Motions," *AIAA Journal*, Vol. 23, No. 8, 1985, pp. 1141, 1142.

[4] Francis, M. S., and Keese, J. E., "Airfoil Dynamic Stall Performance with Large-Amplitude Motions," *AIAA Journal*, Vol. 23, No. 11, 1985, pp. 1653–1659.

[5] Green, R. B., Galbraith, R. A. McD., and Niven, A. J., "Measurements of the Dynamic Stall Vortex Convection Speed," 17th European Rotorcraft Forum, Paper 91-68, Berlin, Sept. 1991.

[6] Tuncer, I. H., Wu, J. C., and Wang, C. M., "Theoretical and Numerical Studies of Oscillating Airfoils," *AIAA Journal*, Vol. 28, No. 9, 1990, pp. 1615–1624.

[7] Visbal, M. R., "Dynamic Stall of a Constant-Rate Pitching Airfoil," *Journal of Aircraft*, Vol. 27, No. 5, 1990, pp. 400–407.

[8] Reu, T., and Ying, S. X., "Hybrid Grid Approach to Study Dynamic Stall," *AIAA Journal*, Vol. 30, No. 11, 1992, pp. 2670–2676.

[9] Tuncer, I. H., Ekaterinaris, J. A., and Platzer, M. F., "Viscous/Inviscid Interaction Method for Unsteady Low-Speed Airfoil Flows," *AIAA Journal*, Vol. 33, No. 1, 1995, pp. 151–154.

[10] Shih, C., Lourenco, L., VanDommelen, L., and Krothapalli, A., "Unsteady Flow Past an Airfoil Pitching at a Constant Rate," *AIAA Journal*, Vol. 30, No. 5, 1992, pp. 1153–1161.

[11] Spalart, P. R., "Vortex Method for Separated Flows," NASA TM 100068, June 1988.

[12] Chorin, A. J., "Numerical Study of Slightly Viscous Flow," *Journal of Fluid Mechanics*, Vol. 57, No. 4, 1973, pp. 785–796.

[13] Angell, R. K., Musgrove, P. J., and Galbraith, R. A. McD., "Collected Data for Tests on a NACA0015 Aerofoil," Dept. of Aerospace Engineering, Univ. of Glasgow, G. U. Aero Rept. 8803, Glasgow, Scotland, UK, 1988.

[14] Vezza, M., "A New Vortex Method for Modelling Two-Dimensional Unsteady Incompressible Viscous Flows," Dept. of Aerospace Engineering, Univ. of Glasgow, G. U. Aero Rept. 9245, Glasgow, Scotland, UK, 1992.

[15] Abbott, I. H., and Doenhoff, A. E. V., *Theory of Wing Sections*, Dover, New York, 1959, Appendix 4.

S. Fleeter
Associate Editor